Journal of *Marine Science and Engineering*

MDPI

Article

New Features of Bragg and Non-Polarized Radar Backscattering from Film Slicks on the Sea Surface

Stanislav Aleksandrovich Ermakov [1,2], Irina Andreevna Sergievskaya [1,2,*], Leonid Mikhailovich Plotnikov [1,2], Ivan Aleksandrovich Kapustin [1,2], Olga Arkadyevna Danilicheva [1,2], Alexander Viktorovich Kupaev [1,2] and Alexander Andreevich Molkov [1,2]

[1] Institute of Applied Physics RAS, Nizhny Novgorod, 46 Ul'yanov Street, 603950 Nizhny Novgorod, Nizhny Novgorod Region, Russia
[2] Volga State University of Water Transport, Nizhny Novgorod, 5 Nesterova Street, 603950 Nizhny Novgorod, Nizhny Novgorod Region, Russia
* Correspondence: i.sergia@ipfran.ru

Abstract: Suppression of radar backscattering from the sea surface has been studied in field experiments with surfactant films carried out from an Oceanographic Platform on the Black Sea and from onboard a research vessel on the Gorky Water Reservoir using an X-C-S-band two co-polarized radar instrument. Bragg and non-polarized (non-Bragg) radar backscatter components, BC and NBC, respectively, were retrieved when measuring the radar backscatter at vertical (VV-) and horizontal (HH-) polarizations. New features of microwave backscattering from the sea surface have been revealed, including a non-monotonic dependence of radar backscatter suppression (contrasts) in slicks on azimuth angle and particularities of BC contrasts on radar wave number. Namely, it is demonstrated that the backscatter contrasts achieve maximum values at azimuth angles in between the upwind and crosswind radar look directions, and BC contrasts increase with radar wave number along the wind and decrease in the crosswind directions. The suppression of BC is discussed in the frame of Bragg's theory of microwave scattering and of a simple model of the wind wave spectrum, while the suppression of NBC is considered associated with the micro-breaking of wind waves. The obtained new features of radar contrasts can be used for the identification and characterization of marine films.

Keywords: sea surface; film slicks; microwave radar backscattering; Bragg and non-Bragg radar return; Doppler shifts

Citation: Ermakov, S.A.; Sergievskaya, I.A.; Plotnikov, L.M.; Kapustin, I.A.; Danilicheva, O.A.; Kupaev, A.V.; Molkov, A.A. New Features of Bragg and Non-Polarized Radar Backscattering from Film Slicks on the Sea Surface. *J. Mar. Sci. Eng.* **2022**, *10*, 1262. https://doi.org/10.3390/jmse10091262

Academic Editor: Charitha Pattiaratchi

Received: 20 July 2022
Accepted: 5 September 2022
Published: 7 September 2022

1. Introduction

The problem of detection of marine films is very important in the context of the ocean ecological monitoring for detection and identification of sea surface pollutions, including wastewater and riverine discharges, biogenic pollutions, oil/oil product spills, etc. (see, e.g., [1–6]). One of the most effective tools for such monitoring is microwave synthetic aperture radar (SAR), which is able to acquire high-resolution images of marine slicks on the sea surface around the clock in various weather conditions (see [7–16] and references therein). The problem of marine film detection is still far from a solution. This is because the mechanisms of microwave radar backscattering, as well as the mechanisms of formation of the spectrum of short, centimeter-decimeter (cm-dm-) scale wind waves, which are primarily responsible for microwave scattering, are not yet fully understood.

Several models of microwave scattering from the sea surface have been developed, including a small perturbation (Bragg) scattering model, a two-scale model, a quasi-specular or Kirchoff model, a small-slope approximation model, and some others (see, e.g., [17–23]). One of the most common is the two-scale model, which combines the Bragg theory with the effects of radar backscatter modulation due to long surface waves [17,18]; however, the existing theories cannot explain some experimental results, for example, strong spikes

in radar backscatter, the cascade backscatter modulation, the discrepancy between polarization ratio values in the experiment and in the two-scale model, etc. [24–26], which are associated, in particular, with nonlinear effects in wind waves: high wave steepness, strong breaking (spilling or plunging) of meter-scale waves, nonlinear structures –parasitic ripples and toe/bulge structures on the cm-dm-scale wave profile, etc. (see, [27–31], and also [32] for more references). The hydrodynamics of nonlinear waves is still insufficiently studied, and the same can be said about the mechanisms of microwave scattering on nonlinear wave structures. This is one of the reasons that empirical and semi-empirical scattering models have been actively elaborated during the last decade (see [33–40] and references therein).

Another part of the problem of microwave scattering on the sea surface is that the spectrum of wind waves and mechanisms of its formation, including sources, sinks, and nonlinear wave effects in the wind wave field, have been insufficiently studied, particularly for short, cm-dm-scale waves, which are mostly responsible for microwave scattering. In particular, if we talk about scattering on the sea surface covered with surfactant films, then the mechanisms of wave attenuation due to films and their relation to the physical characteristics of films remain partly unresolved, despite numerous studies in this area (see, [41,42] for references).

To understand better the processes of formation of the spectra of wind waves, their variability under the action of marine films and, accordingly, the manifestations of the films in radar panoramas of the sea surface, it is very important to conduct controlled experiments on radar probing of surface films with known characteristics. A number of radar experiments have been carried out (see, e.g., [7,8,12,16,43–46]), although the information about film imaging is still scarce. One of the unresolved questions is the dependence of radar backscatter contrasts on the azimuth angle between the radar look and wind velocity directions. In the literature, they either supposed the damping ratio was quasi-isotropic or noticed that the available data were insufficient to draw any conclusions about the angular dependence [6,43,44]. Radar backscatter contrasts in different radar bands and polarizations were studied in the literature (see, [6,8,11,12,14,15]) and were found to grow with radar wave number, although in some works (see, e.g., [7]), the contrast maximum in C- or X-band was obtained. These inconsistencies occurred, as can be assumed since the suppression mechanisms and their effectiveness depending on environmental conditions were poorly understood.

Recently, a new approach was developed in which the radar backscatter was divided into two components—Bragg (BC) and non-polarized ones (see, [34–36]). This approach was expected to provide a better understanding of the nature of radar backscatter and of the different origins of microwave scatterers. It was hypothesized that short, cm- to mm-scale wind waves provide Bragg scattering component for S-to-Ka-bands, while non-polarized scattering is determined by nonlinear structures (spilling/plunging breakers, toe/bulges, parasitic ripples) on the profile of longer, dm-m-scale steep waves. In our last studies [16,46,47], this approach was applied to study the action of films on Bragg and non-polarized backscatter.

The objective of this study is to investigate the damping effect of films on microwave radar backscatter, in particular, to understand better the dependences of radar suppression in film slicks on radar wave number and on azimuth angle. The approach, as mentioned above, is based on the use of a co-polarized X-/C-/S-band microwave radar, which allowed us to retrieve Bragg and non-Bragg scattering components and analyze their variations in slicks. The paper extends the results of our previous experiments by providing new data and demonstrates new peculiarities of the suppression of BC and NBC in the presence of surface films. Particular attention is paid to studying the microwave backscattering in the crosswind radar look direction in order, firstly, to verify and expand the preliminary results of [16,44,45] and, secondly, to better compare the new results with theory and analyze how the model can be further developed. An important new aspect of the presented experiments is the angular dependence of Bragg and non-Bragg backscatter, which has not been practically studied before. The paper is organized as follows. Section 2 presents some

theoretical background on the separation of Bragg and non-polarized components in total radar backscatter. The experiments and experimental procedure are described in Section 3. Experimental results are described in Section 4. Analysis of the result and discussion are presented in Section 5. Concluding remarks are given in Section 6.

2. Theoretical Background

We suppose that microwave scattering is composed of resonance (Bragg) and non-Bragg components. The first component is determined by surface waves, the lengths of which satisfy the resonance with the lengths of electromagnetic waves. The second, non-Bragg (or non-polarized) component is associated with scattering from small quasi-specular facets on the profile of surface waves longer than Bragg ones; the structures appear due to wave nonlinearity, in particular, wave breaking.

The total radar backscatter σ^0_{pp} (or the normalized radar cross section, NRCS) can be written as follows (see, e.g., [34,36])

$$\sigma^0_{pp} = \sigma^0_{B\_pp} + \sigma^0_{NBC} \tag{1}$$

where σ^0_{pp} is the total NRCS, p denotes vertical (V) or horizontal (H) transmit/receive polarizations, $\sigma^0_{B\_pp}$ is the Bragg (polarized) component of radar backscatter described by the two-scale Bragg model, σ^0_{NBC} is the non-polarized (non-Bragg) component. The Bragg component, according to the two-scale radar model, can be written as (see, e.g., [17])

$$\sigma^0_{BC\_pp} = 16\pi k^4_{em} R_{pp}(\theta) F(\vec{k_B}) \tag{2}$$

where $F(\vec{k_B})$ is the spectrum of wind waves at the Bragg wave vector $\vec{k}_B = 2k_{em}\vec{n}_s$, k_{em} is the wave number of an incident electromagnetic wave, $\vec{n}_s$ is a projection of the unit wave vector of an incident electromagnetic wave on the sea surface, $\left|\vec{n}_s\right| = \sin\theta$, θ is the incidence angle, $R_{pp}(\theta)$ is the reflection coefficient which depends on polarizations of the incident/reflected electromagnetic waves.

Assuming that the non-Bragg component is non-polarized, i.e., does not depend on polarization, one can remove NBC from the total radar backscatter (1) when subtracting σ^0_{HH} from σ^0_{VV}. Thus obtained polarization difference (PD) can be described by the two-scale scattering theory as follows

$$PD = \sigma^0_{B\_VV} - \sigma^0_{B\_HH} = 16\pi k^4_{em}(R_{VV} - R_{HH}) F(\vec{k}_B) \tag{3}$$

The non-Bragg component can be found from ((1)–(3)) as

$$\sigma^0_{NBC} = \frac{1}{2}[\sigma^0_{VV} + \sigma^0_{HH} - \frac{R_{VV} + R_{HH}}{R_{VV} - R_{HH}} PD] \tag{4}$$

The polarization ratio (PR) is introduced as

$$PR = \sigma^0_{VV}/\sigma^0_{HH} \tag{5}$$

PR characterizes the contribution of non-polarized scattering to the total radar return. This contribution can be estimated by comparing the experimental PR-values with those predicted by the two-scale Bragg theory.

The suppression degree (contrast) of radar backscatter and of Bragg and non-Bragg components can be defined as

$$K_{pp} = \frac{\sigma^0_{pp\_nonslick}}{\sigma^0_{pp\_slick}}, K_{BC} = \frac{PD_{nonslick}}{PD_{slick}}, K_{NBC} = \frac{\sigma^0_{NBC\_nonslick}}{\sigma^0_{NBC\_slick}} \tag{6}$$

It follows from (2) and (6) that the BC contrast is equal to the ratio of the wind wave spectrum at a corresponding Bragg wave number, i.e.,

$$K_{BC} = \frac{F_0(k_B)}{F_{slick}(k_B)} \tag{7}$$

Radar Doppler shifts F_D are defined as the centroids of the radar backscatter Doppler spectrum $S_j(f)$, namely

$$F_{D_j} = \frac{\int f S_j(f) df}{\int S_j(f) df} = \frac{\int f S_j(f) df}{\sigma_j^0} \tag{8}$$

where j denotes VV-polarized or HH-polarized backscattering, or BC/NBC backscatter components. Since the frequencies can be either above or below the frequency of the incident microwaves depending on whether the scattering elements on the sea surface move toward or away from the radar, the Doppler shifts should be found by integrating separately over positive and negative frequencies.

The velocity projection $\vec{V}_{s,j}\vec{n}_s$ of microwave scatterers on the wave vector $\vec{k}_B = 2k_{em}\vec{n}_s$ can be found from radar Doppler shifts as

$$\vec{V}_{s,j}\vec{n}_s = 2\pi F_{Dj}/k_B \tag{9}$$

It can be obtained easily from (1)–(5) and (8), (9), that the scatterer's velocities for BC and NBC are related to the velocities of VV- and HH-polarized scatterers as

$$V_{s,BC} = \frac{V_{VV}\sigma_{VV} - V_{HH}\sigma_{HH}}{(\sigma_{VV} - \sigma_{HH})} \tag{10}$$

and

$$V_{s,NBR} = \frac{V_{VV}\sigma_{VV} - V_{HH}\sigma_{HH} \cdot R}{(\sigma_{VV} - \sigma_{HH} \cdot R)} \tag{11}$$

respectively, where

$$R = R_{VV}/R_{HH} \tag{12}$$

3. Experiment

The experiments were carried out in 2021 on the Black Sea from an Oceanographic Platform of the Marine Hydrophysical Institute (MHI) and on the Gorky Water Reservoir (GWR) from onboard a research vessel (RV). Dual co-polarized (VV/HH polarizations) X-/C-/S-band Doppler radar was mounted at heights of about 14 m on the Platform and 7 m on the RV (see Figure 1). In the platform experiments, the incidence angles were 50° and 60°, while on the research vessel, it was 60°. The radar antenna beam widths are slightly different in different bands, and corresponding footprints on the water surface were less than 2 m. The X-/C-/S-band radar is a pulse system that simultaneously records the intensity of radar return, radar Doppler spectrum, and speeds of radar scatterers in these three bands and at two co-polarizations (VV and HH). A pulse regime of radar operation allows us to strobe the backscattered signal by distance within a pulse, i.e., to choose a part of the irradiated area on the surface.

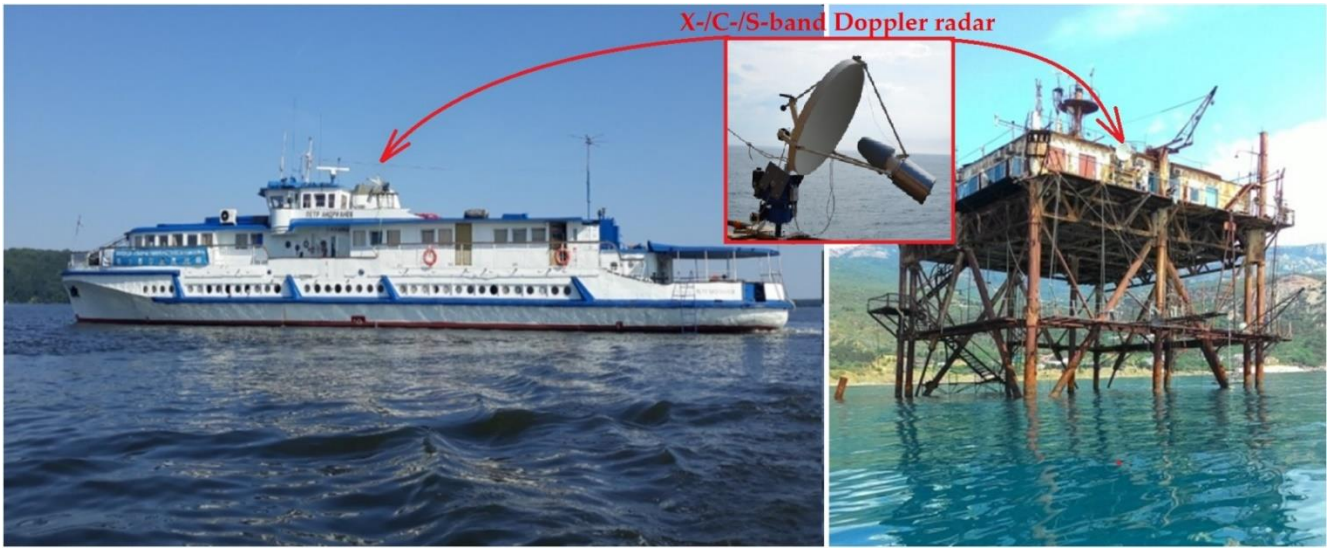

Figure 1. X-/C-/S-band radar mounted onboard the research vessel and the platform.

Scatterer's velocities can be retrieved from the Doppler spectrum as the spectrum centroid. The radar emits and receives pulses in S-, C-, and X-bands, and after receiving a certain number of pulses, it processes the data for some time. The typical pulse frequency was chosen at about 500 Hz and the number of analyzed pulses was about 256, thus providing sufficient frequency resolution in the Doppler spectrum in all the bands. In this regime, the time interval for analyzing the Doppler spectrum was about 0.5 s, and the total time for obtaining the intensities and velocities in three bands and at 2 polarizations was about 4 s.

One should remind that at high enough wind speeds, long waves are present on the sea surface, modulating the short-wave part of the wave spectrum and, correspondingly, the radar backscatter. As a result, the estimated Doppler shifts depend on the Doppler spectrum averaging time and on the modulation intensity of the reflected radar signal. The Doppler shifts of the average spectrum obtained in this way are generally larger than the average instantaneous shifts. For the selected mode of operation of the radar, this led to some, but rather small, increase in Doppler shifts (see also [47]).

Wind speed at the height of 15 m and marine currents were measured from the platform with an ultrasonic anemometer and a Doppler acoustic current meter, respectively.

The experiments were carried out with artificial surfactant films with pre-measured characteristics. Here we report only on measurements using oleic acid (OLE). Film slicks during our experiments were created with solutions of OLE in pure ethanol poured onto the water surface. Usually, about 1 L of 50% OLE solutions were used, and typical slick dimensions were about 100 m by 300 m. Oleic acid at corresponding surface concentrations forms monomolecular (over)saturated films (the concentration of a saturated monomolecular OLE film is about 1–2 mg/sq.m [48]), which characteristics—the elasticity and surface tension coefficient are nearly constant and, as was obtained in our laboratory studies [48], are about 20–30 mN/m and 30 mN/m, respectively.

The radar Doppler shifts, and the scatterer's velocities were calculated using instantaneous radar spectrum corresponding to a certain distance from the footprint center on sea surface according to the formulas presented in Section 2. Then the Doppler shifts/velocities were averaged over time. One should note that some instantaneous values $\sigma_{VV} - \sigma_{\mathrm{HH}}$ were close to 0 or even negative, although mean values of σ_{VV} are larger than σ_{HH}. This can result in unrealistically high scatterer's velocities and these cases were filtered out from corresponding time series.

4. Results

4.1. Polarization Ratio

An example of time series of VV/HH-polarized radar backscatter is presented in Figure 2. A slick is clearly manifested as strong suppression of the radar backscatter in different radar bands both for VV and HH-polarizations.

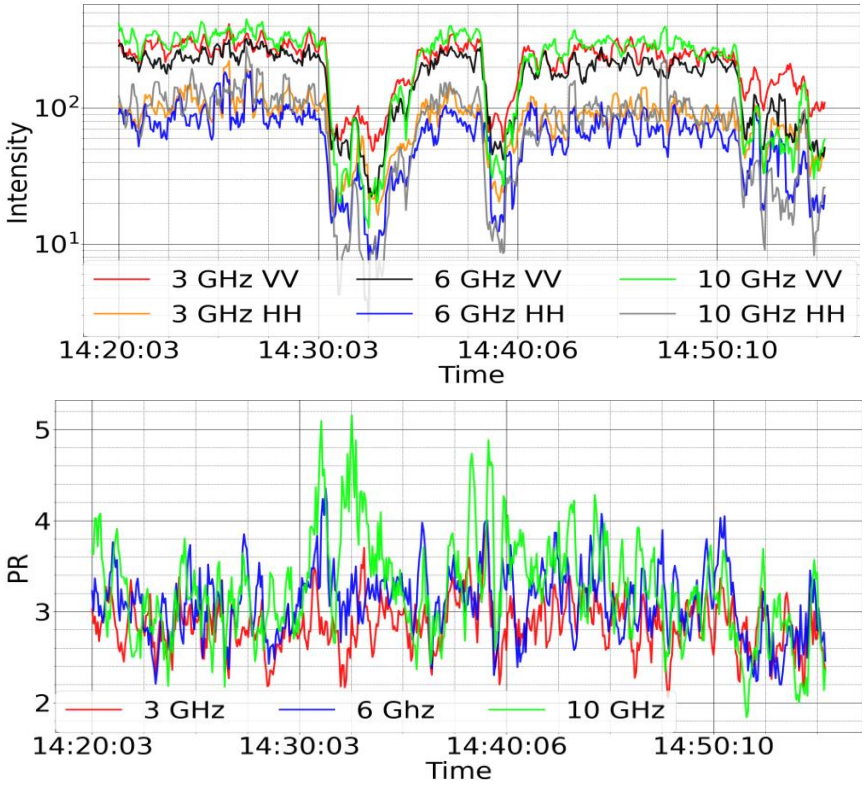

Figure 2. An example of radar backscatter time series in different radar bands and at VV and HH-polarizations and corresponding polarization ratio. Upwind observation.

It is seen that the PR values in slicks can increase somewhat, but not always, indicating that the HH-polarized radar backscatter can be suppressed more than VV-polarized one. In any case, the effect of PR changing in slicks is not sufficiently pronounced. This is illustrated in Figure 3, where PR values in X-, C-, and S-bands as functions of azimuth angle are depicted.

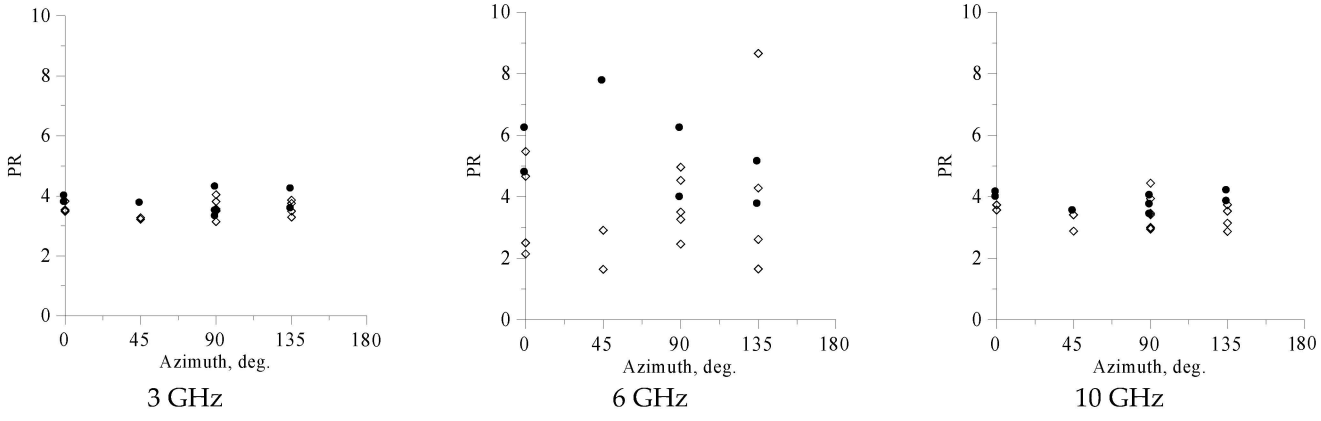

Figure 3. PR for nonslicks and for slicks at an incidence angle of 60°. Open symbols—nonslicks, solid symbols—slicks. GWR, 2021, wind velocity of 5–6 m/s.

Experimental PR-values vary with incidence angle, as shown in Figure 4. The PR-values are shown as functions of Bragg wave number at two incidence angles of 50° and 60°.

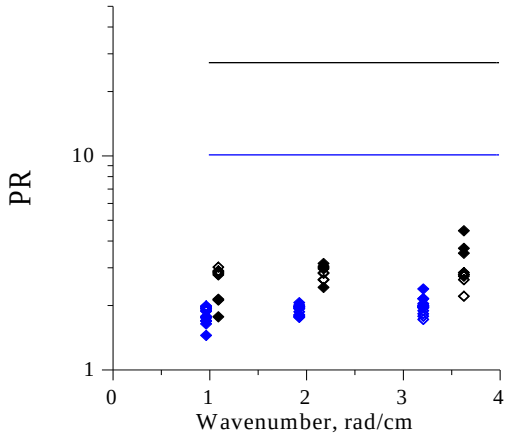

Figure 4. PR for crosswind observations at incidence angles of 50° (blue symbols) and 60° (black symbols). Open and solid diamonds—slick and non-slick areas, respectively. Colored lines are Bragg PR-values at corresponding incidence angles.

It is seen that the PR-values are about or greater than 1, but significantly less than that predicted by Bragg's theory. Namely, according to Bragg's theory, the PR-values for the conditions of our experiments are about 25 and 10 at incidence angles of 60° and 50°, respectively, so that non-polarized scattering contributes noticeably to the total backscatter. As mentioned above, there is a small difference between PR values for non-slicks and slicks. Some small increase in PR in slicks, e.g., in the X-band, can be explained by the fact that VV-polarized scattering is determined mainly by cm-scale GCW, while HH-polarized scattering is mostly due to sharp wave crests or other nonlinear features of longer, dm-scale GCW, resulting is quasi specular reflections (see, [16,26,47]). The nonlinear structures can be more sensitive to suppression (even if the latter is small) of dm-scale GCW than cm-scale waves, so the HH-polarized NRCS is suppressed stronger than VV-polarized, and PR in slicks can slightly increase.

4.2. Contrasts

Next, we present BC and NBC contrasts in slicks in order to understand better the nature of different scatterers, which, as mentioned above, are cm-scale Bragg waves for BC and presumably nonlinear features on the dm-scale GCW for NBC. Typical BC and NBC contrast obtained in the experiments on GWR for the case of radar probing in upwind, crosswind, and 45° directions relative to wind velocity are shown in Figure 5.

It is seen that for upwind observations, NBC contrasts are slightly stronger than those of BC, and both BC and NBC contrasts tend to increase with wave number.

BC and NBC contrasts in the upwind direction are consistent, in general, with those in our previous studies growing with wave number (see, e.g., [16]). A similar behavior is observed for 45° contrasts, although they are noticeably larger than for the upwind direction.

The contrasts in the crosswind direction demonstrate a completely different behavior, namely: BC contrasts decrease or almost do not change with wave number, while the NBC contrasts increase as in the case of observations along the wind.

More data on the crosswind slick contrasts were obtained in experiments in 2021 from the Oceanographic Platform on the Black Sea. The results are shown in Figure 6.

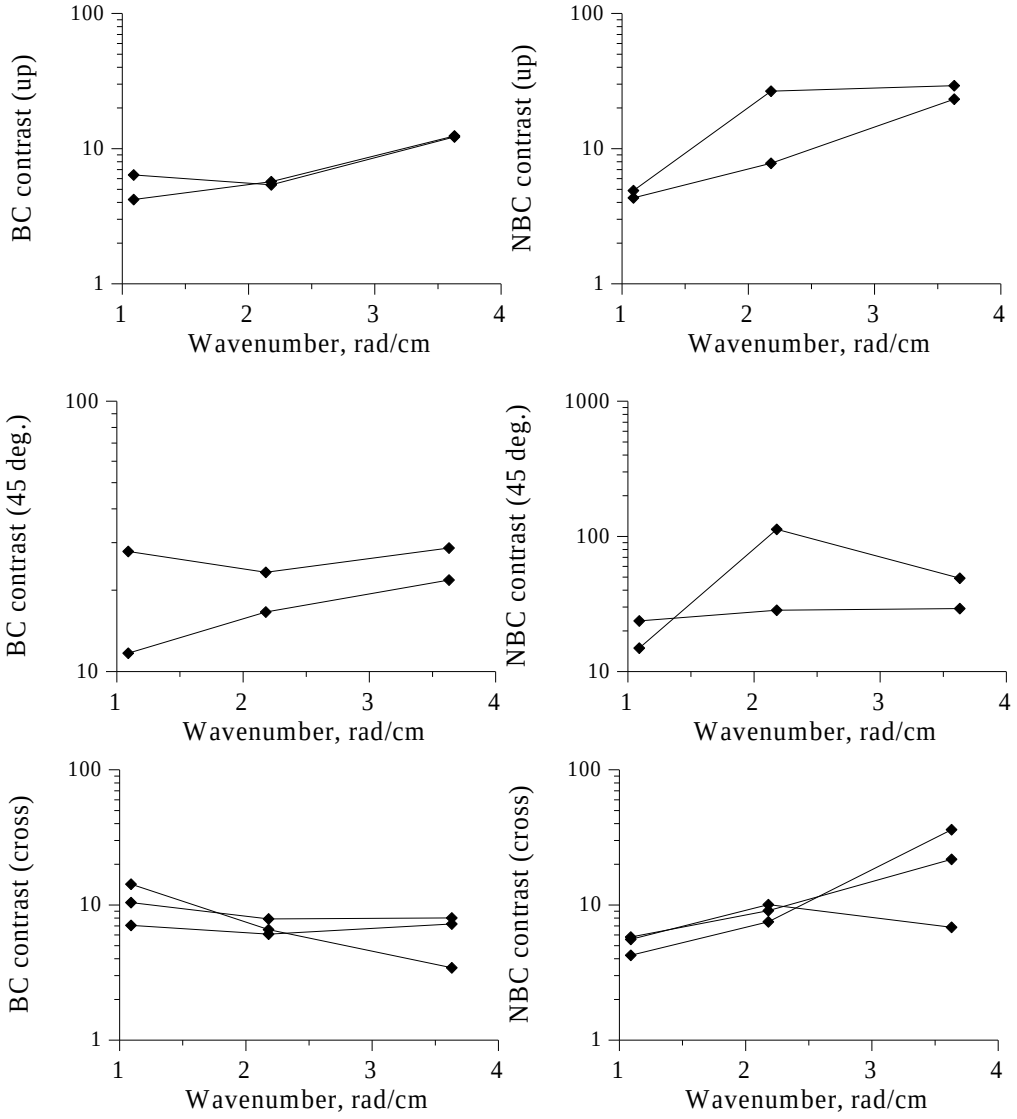

Figure 5. BC and NBC contrasts at different azimuth angles as functions of radar Bragg wavenumber. GWR, wind velocity of 5–6 m/s.

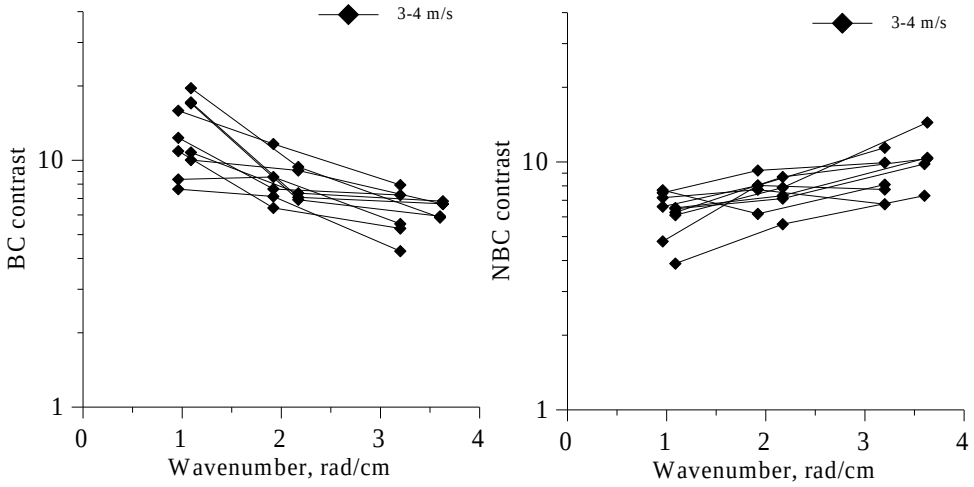

Figure 6. BC and NBC cross wind contrasts vs. Bragg wave number. The Black Sea, wind velocity of 3–4 m/s, incidence angles of 50° and 60°.

As we mentioned above, the contrasts in the direction of 45° are several times greater than the upwind and crosswind contrasts, both for BC and NBC. This feature of the angular dependence of radar contrasts is best illustrated in Figure 7, where more data are used. One should remind that the azimuth angle between wind velocity and radar look directions, in our notations, is zero for the upwind direction, and 180° for downwind observations, i.e., when the radar look and the wind velocity directions coinside. Figure 7 clearly shows that both BC and NBC contrasts at azimuth angles of about 45° and 135° degrees are greater than the contrasts for up-/crosswind directions. As far as we know, this feature has not been reported in the literature.

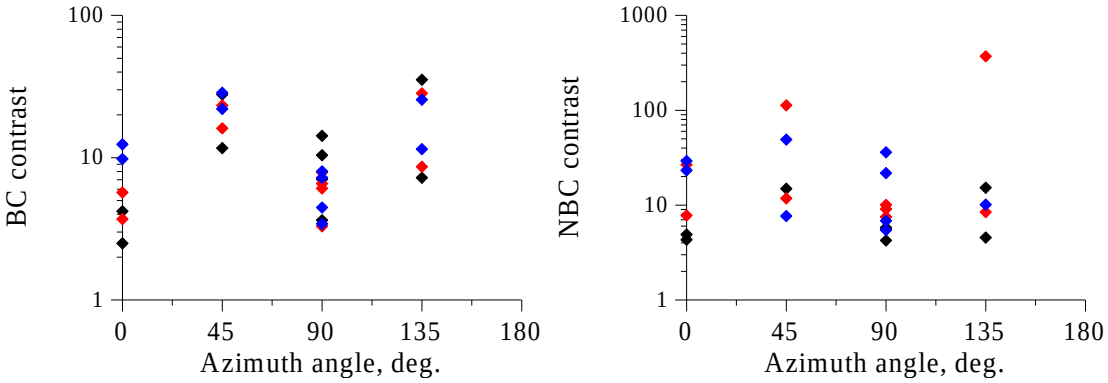

Figure 7. BC (**left panel**) and NBC (**right panel**) contrasts vs. azimuth angle (0°—upwind, 90°—crosswind). GWR 19.08.2021. Black symbols—S-band, red—C-band, and blue—X-band. Wind velocity 5–6 m/s.

4.3. Radar Doppler Shifts

Here we present the results of studying the radar Doppler spectra and radar Doppler shifts measured from an Oceanographic Platform in 2021 and of data processing of similar previous experiments. Radar Doppler spectra obtained in our boat experiments on GWR are more difficult to process and interpret due to the boat movement, since the latter was often quite variable.

Some examples of the radar Doppler spectra at different azimuth angles are shown in Figure 8. The spectra contain two parts: one corresponds to waves traveling along the wind (negative frequencies in our notations) and the other to waves propagating in the direction opposite to the wind (positive frequencies).

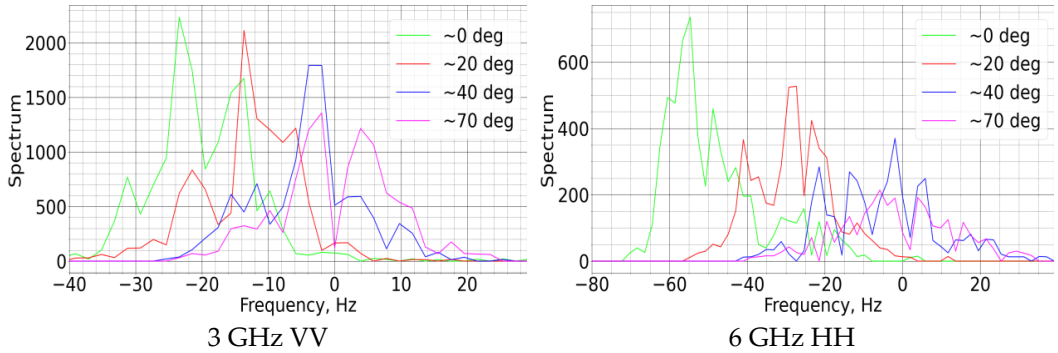

Figure 8. Some examples of the Doppler spectra of radar backscatter at different azimuth angles. Oceanographic Platform, the Black Sea.

At small azimuth angles, the waves moving against the wind are obviously weak and the Doppler spectrum centroid (the Doppler shift) for these waves is difficult to find accurately enough. The negative Doppler shifts in Figure 9 at azimuth angles less than 90° correspond to waves propagating downwind and towards radar, while the positive shifts

correspond to waves traveling against the wind. The Doppler peak for the last waves is much smaller than for the waves along the wind, thus indicating that the waves moving against the wind are small compared to downwind waves. When the radar look-direction is larger than 90°, then the situation is reversed, and positive Doppler shifts correspond to waves traveling from the radar roughly along the wind. BC and NBC Doppler shifts are shown in Figure 9. The Doppler shifts are not symmetric relative to zero; this may be due to the wind drift velocity. After subtracting the Doppler shift caused by the wind, assuming the wind drift as 3% of the wind speed, the Doppler shifts become symmetrical (see below).

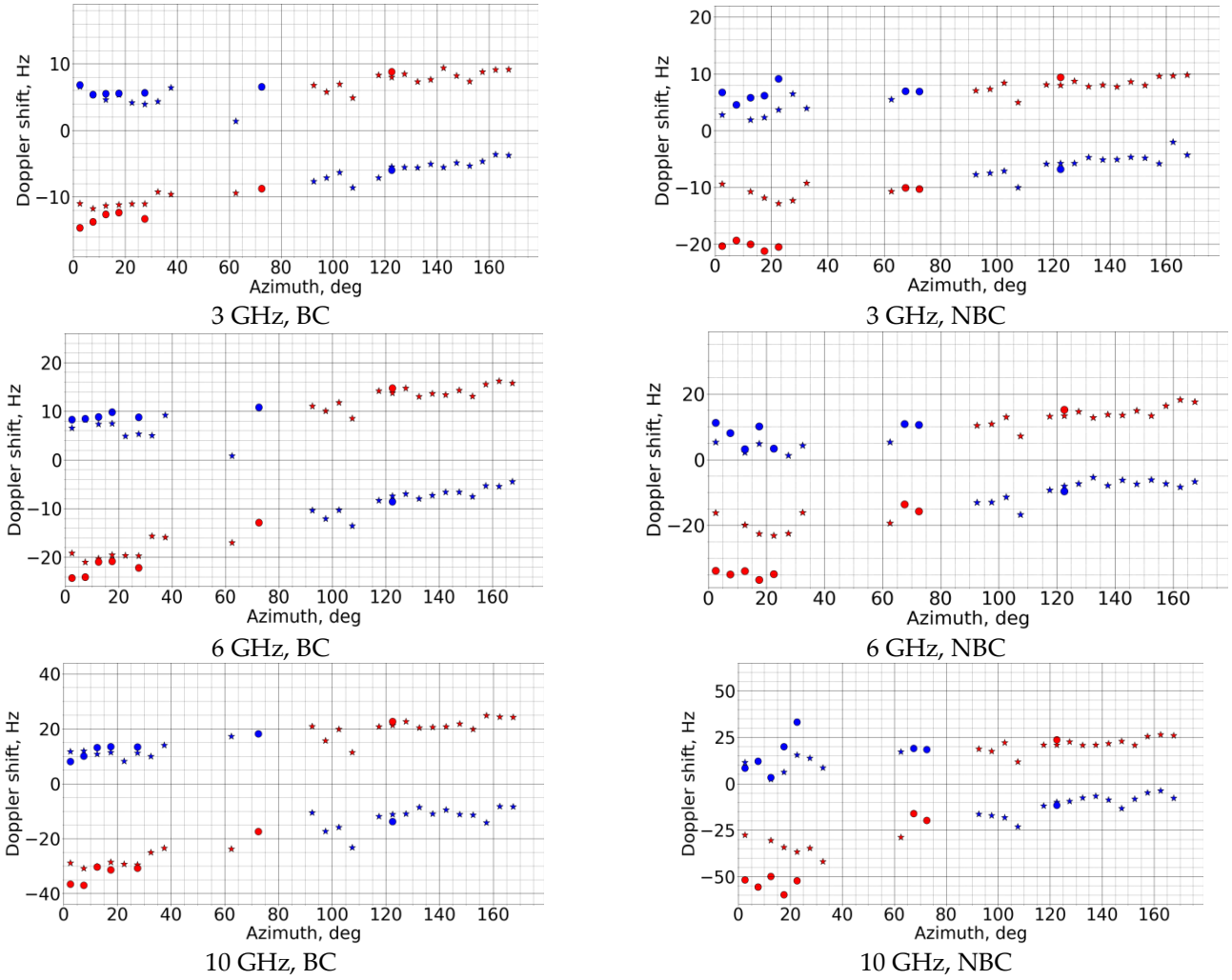

Figure 9. Radar Doppler shifts for BC and NBC as functions of azimuth angle. Red symbols—scatterers moving downwind, blue symbols—against the wind, stars, and circles correspond to wind velocities of 6–7 m/s, and 10–11 m/s, respectively.

5. Discussion

Let us consider first the radar Doppler shifts for both BC and NBC components which may help in the understanding of the nature of BC and NBC scatterers. After subtracting from the BC and NBC Doppler shifts, the component associated with the wind drift velocity, estimated as 3% of wind speed, and recalculating the Doppler shift into scatterers velocities V_s as

$$V_s = 2\pi F_{D(BC/NBC)}/k_B - V_{drift}\cos\varphi \quad (13)$$

where φ denotes the azimuth angle; we arrive at the scatterer's velocities, as shown in Figure 10. Theoretical lines are also shown in Figure 10, denoting the velocities of linear cm-scale gravity-capillary waves (GCW) corresponding to Bragg waves for X-, C-, and

S-bands. We can conclude that the scatterer's velocities for upwind radar probing are somewhat larger, particularly for NBC scatterers, than the velocities described by the dispersion relation of gravity-capillary waves. This can occur because of the contribution of the scatterers associated with nonlinear longer and faster moving decimeter-meter-scale waves. At azimuth angles close to 90 degrees, the estimated BC scatterer's velocities are closer, although still a little larger, to the velocities of linear GCW (see Figure 11).

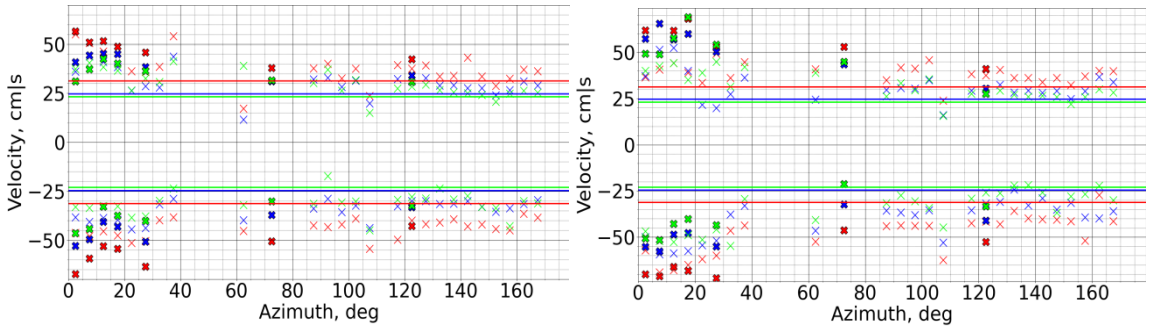

Figure 10. Velocities of BC (**left**) and NBC (**right**) scatterers (red crosses 3 GHz, blue—6 GHz, green −10 GHz at wind velocities about 6 m/s, colored squares—for wind velocities 10–11 m/s).

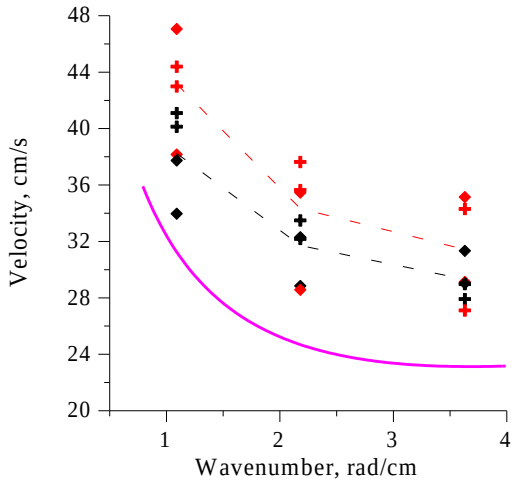

Figure 11. BC and NBC scatterer velocities (black and red symbols, respectively) for a crosswind direction. Solid line is the phase velocity of linear gravity-capillary waves. Dashed lines denote the best fit of experimental data.

When considering the obtained radar Doppler shifts, it can be concluded that the BC scatterers can be approximately described as weakly nonlinear GCW whose phase velocities are close to the linear dispersion relation. Since GCW can hardly be generated by the wind perpendicular to wind direction, we can assume that these wave components are generated due to weak wave–wave interactions, the result of which is a small difference in wave velocities from their linear values (see, e.g., [38,49]).

Under this assumption, we can describe BC scatterers in the frame of a kinetic equation for the spectrum $F(\vec{k}, \vec{x}, t)$ of gravity-capillary waves (see, e.g., [50,51])

$$\frac{\mathrm{dF}(\vec{k}, x, t)}{\mathrm{dt}} = Q[F, \vec{k}, u*, \gamma(k, E, \sigma, \dots)] \tag{14}$$

with the r.h.s. describing wind wave energy sources, sinks, and nonlinear wave effects. In particular, Q should contain nonlinear terms describing weakly nonlinear wave–wave interactions, as well as strongly nonlinear processes such as wave breaking, responsible, among

others, for the wind wave spectrum limitation. Wave–wave interactions are described by a collision integral which is extremely difficult to analyze. Wave breaking processes are also studied insufficiently, and no analytical approach to their description; therefore, these complicated nonlinear processes are described by some empirical, usually algebraic expressions. The equilibrium spectrum of wind waves $F(\vec{k})$ can be found when equating the r.h.s. of (14) to 0.

The most common expression for Q used in the literature can be written as (cf., [34])

$$Q(F, u*, \gamma(k, E, \sigma, \nu \ldots), \varphi, \ldots) = \beta_{eff} N(k) + P_a(k, V_{wind}) - F(k)\left(\frac{F(k)}{\alpha(k)}\right)^n + I[F(k_l)] \quad (15)$$

where $\beta_{eff} = \beta(\vec{k}, u*) - 2 \cdot \gamma(k, E, \sigma, \nu, \ldots)$, $\beta(\vec{k}, u*, \varphi)$ is the wind growth rate due to the Miles excitation mechanism (see an expression for $\beta(k, u*, \varphi) = \beta(k, u*) \cos^2 \varphi$ in [52]), φ is an angle between the wind velocity and the wave vector, P_a is the source of wind waves due to atmospheric pressure pulsations—the Phillips mechanism, [50]), both the wave generation mechanisms depend on φ and are inefficient for crosswind propagating waves, $u*$ is the wind friction velocity, $\gamma(k, E, \sigma, \nu, \ldots)$ the wave damping coefficient, which depends on the film elasticity E, surface tension σ, water viscosity ν, and some other surfactant film characteristics, e.g., film viscosity, thickness, etc. (see [41,42] and cited literature). The third term is introduced to describe in a simple way the processes of nonlinear spectrum limitation due to, in particular, wave breaking; here $\alpha(k)$ and n are some empirical values. In order to describe the wind wave excitation in the cross wind direction when the Miles and Phillips mechanisms are not acting, we also introduced an additional phenomenological term $I[F(k_l)]$ describing the wave excitation due to wind waves with wave numbers other than k, ($k_l < k$). Following [34,35], one can suppose that k_l can be associated with dm-m-scale wind waves.

Then when assuming that nonlinear interactions are weakly modified by film, the BC contrast can be written in the simplest form as

$$K_{BC}(\phi = 90^\circ) = \frac{F_0(k_B)}{F_{sl}(k_B)} = \frac{I[k, F(k_l)]_{nonslick}}{I[k, F(k_l)]_{slick}} \frac{\gamma_{slick}}{\gamma_{nonslick}} \approx \frac{\gamma_{slick}}{\gamma_{nonslick}} \quad (16)$$

The last equality in (16) can be written to neglect the influence of films on the wave source $I[F(k_l)]$.

Formula (16) can be considered as a particular case of a local balance model previously used to describe contrasts in slicks for arbitrary, but not crosswind, look directions. The BC contrast can be expressed as follows (see, [43,44])

$$K_{BC} = \left[\frac{[\beta(u_*, k, \varphi) - 2\gamma(k, E, \sigma)]_{nonclick}}{[\beta(u_{*sl}, k, \varphi) - 2\gamma(k, E, \sigma)]_{slick}}\right]^n \; n = 1, \text{ if } \beta_{eff} > 0; \; n = -1, \text{ if } \beta_{eff} < 0 \quad (17)$$

Let us now compare the BC contrasts in the crosswind direction with the simple model above. We can supplement the data for 2021 with those obtained in our earlier observations, as shown in Figure 12. The figure summarizes the crosswind BC contrasts at wind velocities in the range from approximately 3 m/s to 6 m/s. No significant dependence on wind speed is observed within the studied wind velocity range. The OLE film elasticity, according to [48], is within the range shown in Figure 12. One can conclude from Figure 12 that the simple model (16) agrees with the experiment, at least within the limits of experimental accuracy.

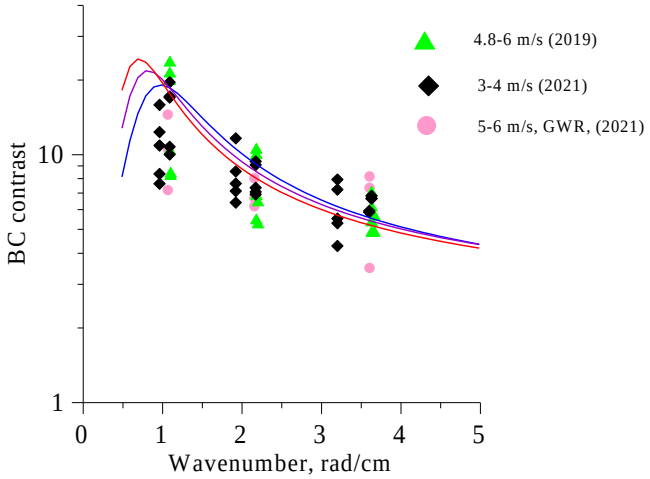

Figure 12. Comparison between experimental BC contrasts for crosswind observations in experiments of 2021 and 2019 (see, [45]) and theory (16) at film elasticity of 20 mN/m, 25 mN/m, and 30 mN/m (blue, violet, and red curves, respectively).

It is seen from Figure 12 that theoretical contrast values in the studied wave number range weakly depend on film elasticity, and therefore, it is difficult to estimate this parameter accurately from the measured contrasts; however, we believe that the crosswind contrast as functions of wave number can be used, at least, for film identification.

Finally, we can compare the angular dependence of BC contrasts (see, Figure 7) with the local balance model. The contrasts calculated according to (17) for the conditions of our experiments are shown in Figure 13, along with the obtained experimental BC contrast values. Although the wave number range of the model is rather limited, as is seen in Figure 13, nevertheless, the model correctly predicts the tendency of the contrast to increase at azimuth angles between 0° and 90°.

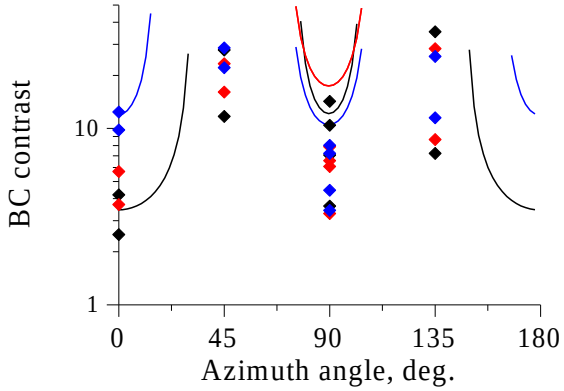

Figure 13. Comparison between experimental BC contrasts (symbols) and a local balance model (curves). Black symbols/curve—S-band, red—C-band, and blue—X-band.

6. Conclusions

Experiments on radar probing of the water surface covered with surfactant films of oleic acid were carried out from an Oceanographic Platform on the Black Sea and from onboard a research vessel on the Gorky Water Reservoir. A three-band dual co-polarized radar of the Institute of Applied Physics operating simultaneously in X-, C-, and S-bands and at VV-and HH-polarizations was used in the experiments. Suppression of radar return in film slicks (contrast), as well as radar Doppler shifts for VV/HH-polarized backscatter and Bragg/non-Bragg (non-polarized) backscatter components, were studied at wind speeds ranging from about 3 to 6 m/s and at incidence angles of microwaves 50° and 60°. New features of microwave backscattering from the sea surface have been revealed. First, a

nonmonotonic dependence of radar backscatter contrasts in slicks on azimuth angle has been revealed. Namely, BC and NBC contrasts achieve maximum values for the radar look directions between the upwind and crosswind directions. Second, BC contrasts demonstrate significantly different dependencies on radar wave numbers, increasing for upwind and decreasing for crosswind directions; NBC contrast grows with wave number for all radar look directions. Finally, the radar Doppler shifts and corresponding scatterer's velocities for upwind and downwind observation directions are found to be somewhat larger than the velocities of linear gravity-capillary waves with Bragg wavelengths corresponding to X-C- and S-bands. For the crosswind direction, scatterers' velocities are closer to the Bragg wave velocities, although remaining 15–20% larger than the latter. Nevertheless, we hypothesized that the crosswind BC scatterers could be considered as quasilinear gravity-capillary waves. The spectrum of these waves was described when introducing a phenomenological wave energy source which is balanced by viscous wave damping due to film. The crosswind BC contrast can be found as the ratio of the spectrum of wind waves in nonslicks and slicks, when neglecting the influence of film on the wave source. It turned out under this assumption that the theory agrees well with the experiment, at least under the studied environmental and experimental conditions.

The new features of microwave backscattering revealed in our experiments can be potentially used to develop new methods for film identification.

Author Contributions: Conceptualization, S.A.E. and I.A.S.; methodology, S.A.E. and I.A.S.; investigation, I.A.S. and L.M.P.; data curation, I.A.K., A.V.K., O.A.D. and A.A.M.; writing, S.A.E. All authors have read and agreed to the published version of the manuscript.

Funding: This work was supported by the Ministry of Science and Higher Education of the Russian Federation under Grant 075-15-2020-776.

Institutional Review Board Statement: Not applicable.

Informed Consent Statement: Not applicable.

Data Availability Statement: The reader can ask for all the related data from the corresponding author.

Conflicts of Interest: The authors declare no conflict of interest.

References

1. Bondur, V.G. Satellite monitoring and mathematical modelling of deep runoff turbulent jets in coastal water areas. In *Waste Water-Evaluation and Management*, 1st ed.; Einschlag, F.S.G., Ed.; IntechOpen: London, UK, 2011; pp. 155–180; ISBN 978-953-307-233-3. [CrossRef]
2. Bondur, V.G.; Vorobjev, V.E.; Grebenjuk, Y.V.; Sabinin, K.D.; Serebryany, A.N. Study of fields of currents and pollution of the coastal waters on the Gelendzhik Shelf of the Black Sea with space data. *Izv. Atmos. Ocean. Phys.* **2013**, *49*, 886–896. [CrossRef]
3. Pugach, S.P.; Pipko, I.I.; Shakhova, N.E.; Shirshin, E.A.; Perminova, I.V.; Gustafsson, O.; Bondur, V.G.; Ruban, A.S.; Semiletov, I.P. Dissolved organic matter and its optical characteristics in the Laptev and East Siberian seas: Spatial distribution and interannual variability (2003–2011). *Ocean. Sci. J.* **2018**, *14*, 87–103. [CrossRef]
4. Bondur, V.G.; Grebenyuk, Y.V.; Ezhova, E.V.; Kazakov, V.I.; Sergeev, D.A.; Soustova, I.A.; Troitskaya, Y.I. Surface manifestations of internal waves investigated by a subsurface buoyant jet: 1. The Mechanism of Internal-Wave Generation. *Izv. Atmos. Ocean. Phys.* **2009**, *45*, 779–790. [CrossRef]
5. Fingas, M.; Brown, C. Review of oil spill remote sensing. *Mar. Pollut. Bull.* **2014**, *83*, 9–23. [CrossRef] [PubMed]
6. Gade, M.; Alpers, W.; Huehnerfuss, H.; Wismann, V.; Lange, P. On the reduction of the radar backscatter by oceanic surface films: Scatterometer measurements and their theoretical interpretation. *Remote Sens. Environ.* **1998**, *66*, 52–70. [CrossRef]
7. Alpers, W.; Hühnerfuss, H. The damping of ocean waves by surface films: A new look at an old problem. *J. Geophys. Res.* **1989**, *94*, 6251–6266. [CrossRef]
8. Gade, M.; Alpers, W.; Hühnerfuss, H.; Masuko, H.; Kobayashi, T. Imaging of biogenic and anthropogenic ocean surface films by the multifrequency/multipolarization SIR-C/X-SAR. *J. Geophys. Res.* **1998**, *103*, 18851–18866. [CrossRef]
9. Da Silva, J.C.B.; Ermakov, S.A.; Robinson, I.S.; Jeans, D.R.G.; Kijashko, S.V. Role of surface films in ERS SAR signatures of internal waves on the shelf. 1. Short-period internal waves. *J. Geophys. Res.* **1998**, *103*, 8009–8031. [CrossRef]
10. Scott, J.C.; Thomas, N.H. Sea surface slicks—Surface chemistry and hydrodynamics in radar remote sensing. In *Wind-Over-Wave Couplings. Perspectives and Prospects*, 1st ed.; Sajjadi, S.G., Thomas, N.H., Hunt, J.C.R., Eds.; Clarendon Press: New York, NY, USA, 1999; pp. 221–229; ISBN 0-19-850192-7.
11. Brekke, C.; Solberg, A.H.S. Oil spill detection by satellite remote sensing. *Remote Sens. Environ.* **2005**, *95*, 1–13. [CrossRef]

12. Minchew, B.; Jones, C.E.; Holt, B. Polarimetric analysis of backscatter from the Deepwater horizon oil spill using L-band synthetic aperture radar. *IEEE Trans. Geosci. Remote Sens.* **2012**, *50*, 3812–3830. [CrossRef]
13. Kudryavtsev, V.N.; Chapron, B.; Myasoedov, A.G.; Collard, F.; Johannessen, J.A. On dual co-polarized SAR measurements of the Ocean surface. *IEEE Geosci. Remote Sens. Lett.* **2013**, *10*, 763–765. [CrossRef]
14. Skrunes, S.; Brekke, C.; Eltoft, T.; Kudryavtsev, V. Comparing near coincident C- and X-band SAR acquisitions of marine oil spills. *IEEE Trans. Geosci. Remote Sens.* **2015**, *53*, 1958–1975. [CrossRef]
15. Hansen, M.W.; Kudryavtsev, V.; Chapron, B.; Brekke, C.; Johannessen, J.A. Wave Breaking in Slicks: Impacts on C-Band Quad-Polarized SAR Measurements. *IEEE J. Sel. Top. Appl. Earth Obs. Remote Sens.* **2016**, *9*, 4929–4940. [CrossRef]
16. Ermakov, S.A.; Sergievskaya, I.A.; da Silva, J.C.B.; Kapustin, I.A.; Shomina, O.V.; Kupaev, A.V.; Molkov, A.A. Remote Sensing of Organic Films on the Water Surface Using Dual Co-Polarized Ship-Based X-/C-/S-Band Radar and TerraSAR-X. *Remote Sens.* **2018**, *10*, 1097. [CrossRef]
17. Valenzuela, G.R. Theories for the interaction of electromagnetic and oceanic waves—A review. *Bound.-Layer Meteorol.* **1978**, *13*, 61–85. [CrossRef]
18. Bass, F.G.; Fuks, M. *Wave Scattering from Statistically Rough Surfaces*; Pergamon: Oxford, UK, 1979; p. 558; ISBN 978-0-08-019896-5.
19. Voronovich, A. Small-Slope Approximation for Electromagnetic Wave Scattering at a Rough Interface of Two Dielectric Half Spaces. *Waves Random Complex Media* **1994**, *4*, 337–367. [CrossRef]
20. Romeiser, R.; Alpers, W.; Wismann, V. An improved composite surface model for the radar backscattering cross section of the ocean surface. 1. Theory of the model and optimization/validation by scatterometer data. *J. Geophys. Res.* **1997**, *102*, 25237–25250. [CrossRef]
21. Voronovich, A.G.; Zavorotny, V.U. Theoretical model for scattering of radar signals in at K $_u$—and C-bands from a rough sea surface with breaking waves. *Waves Random Complex. Media* **2001**, *11*, 247–269. [CrossRef]
22. Churyumov, A.N.; Kravtsov, Y.A.; Lavrova, O.Y.; Litovchenko, K.T.; Mityagina, M.I.; Sabinin, K.D. Signatures of resonant and non-resonant scattering mechanisms on radar images of internal waves. *Int. J. Remote Sens.* **2002**, *23*, 4341–4355. [CrossRef]
23. Bulatov, M.G.; Kravtsov, Y.A.; Lavrova, O.Y.; Litovchenko, K.T.; Mitiagina, M.I.; Raev, M.D.; Sabinin, K.D.; Trokhimovskii, Y.G.; Churyumov, A.N.; Shugan, I.V. Physical mechanisms of aerospace radar imaging of the ocean. *Phys. Uspekhi* **2003**, *46*, 63–79. [CrossRef]
24. Jessup, A.T.; Keller, W.C.; Melville, W.K. Measurements of Sea Spikes in Microwave Backscatter at Moderate Incidence. *J. Geophys. Res.* **1990**, *95*, 9679–9688. [CrossRef]
25. Ermakov, S.A.; Kapustin, I.A.; Sergievskaya, I.A. On peculiarities of scattering of microwave radar signals by breaking gravity-capillary waves. *Radiophys. Quantum Electron.* **2012**, *55*, 453–461. [CrossRef]
26. Sergievskaya, I.A.; Ermakov, S.A.; Ermoshkin, A.V.; Kapustin, I.A.; Molkov, A.A.; Danilicheva, O.A.; Shomina, O.V. Modulation of Dual-Polarized X-Band Radar Backscatter Due to Long Wind Waves. *Remote Sens.* **2019**, *11*, 423. [CrossRef]
27. Longuet-Higgins, M.S. Parasitic capillary waves: A direct calculation. *J. Fluid. Mech.* **1995**, *301*, 79–107. [CrossRef]
28. Fedorov, A.V.; Melville, W.K. Nonlinear gravity-capillary waves with forcing and dissipation. *J. Fluid Mech.* **1998**, *354*, 1–42. [CrossRef]
29. Longuet-Higgins, M.; Cleaver, R. Crest instability of gravity waves. Part 1. The almost highest wave. *J. Fluid Mech.* **1994**, *258*, 115–129. [CrossRef]
30. Duncan, J.H. Spilling breakers. *Annu. Rev. Fluid Mech.* **2001**, *33*, 519–547. [CrossRef]
31. Qiao, H.; Duncan, J. Gentle spilling breakers: Crest flow-field evolution. *J. Fluid. Mech.* **2001**, *439*, 57–85. [CrossRef]
32. Ermakov, S.A.; Sergievskaya, I.A.; Dobrokhotov, V.A.; Lazareva, T.N. Wave Tank Study of Steep Gravity-Capillary Waves and Their Role in Ka-Band Radar Backscatter. *IEEE Trans. Geosci. Remote Sens.* **2021**, *60*, 1–12. [CrossRef]
33. Donelan, M.A.; Pierson, W.J., Jr. Radar scattering and equilibrium ranges in wind-generated waves with application to scatterometry. *J. Geophys. Res.* **1987**, *92*, 4971–5029. [CrossRef]
34. Kudryavtsev, V.; Hauser, D.; Caudal, G.; Chapron, B. A semi-empirical model of the normalized radar cross section of the sea surface. 1. Background model. *J. Geophys. Res.* **2003**, *108*, 8054. [CrossRef]
35. Kudryavtsev, V.; Akimov, D.; Johannessen, J.A.; Chapron, B. On radar imaging of current features. 1. Model and comparison with observations. *J. Geophys. Res.* **2005**, *110*, C07016. [CrossRef]
36. Phillips, O.M. Radar returns from the sea surface—Bragg scattering and breaking waves. *J. Phys. Oceanogr.* **1988**, *18*, 1065–1074. [CrossRef]
37. Ludeno, G.; Raffa, F.; Soldovieri, F.; Serafino, F. Proof of Feasibility of the Sea State Monitoring from Data Collected in Medium Pulse Mode by a X-Band Wave Radar System. *Remote Sens.* **2018**, *10*, 459. [CrossRef]
38. Huang, W.; Liu, X.; Gill, E.W. Ocean Wind and Wave Measurements Using X-Band Marine Radar: A Comprehensive Review. *Remote Sens.* **2017**, *9*, 1261. [CrossRef]
39. Stoffelen, A.; Verspeek, J.A.; Vogelzang, J.; Verhoef, A. The CMOD7 Geophysical Model Function for ASCAT and ERS Wind Retrievals. *IEEE J. Sel. Top. Appl. Earth Obs. Remote Sens.* **2017**, *10*, 2123–2134. [CrossRef]
40. Yurovsky, Y.Y.; Kudryavtsev, V.N.; Grodsky, S.A.; Chapron, B. Ka-band Dual Co-Polarized Empirical Model for the Sea Surface Radar Cross-Section. *IEEE Trans. Geosci. Remote Sens.* **2017**, *55*, 1629–1647. [CrossRef]
41. Sergievskaya, I.; Ermakov, S.; Lazareva, T.; Guo, J. Damping of surface waves due to crude oil/oil emulsion films on water. *Mar. Pollut. Bull.* **2019**, *146*, 206–214. [CrossRef]

42. Rajan, G.K. A three-fluid model for the dissipation of interfacial capillary-gravity waves. *Phys. Fluids* **2020**, *32*, 122121. [CrossRef]
43. Ermakov, S.A.; Zujkova, E.M.; Panchenko, A.R.; Salashin, S.G.; Talipova, T.G.; Titov, V.I. Surface film effect on short wind waves. *Dyn. Atmos. Ocean.* **1986**, *10*, 31–50. [CrossRef]
44. Ermakov, S.A.; Panchenko, A.R.; Salashin, S.G. Film Slicks on the Sea Surface and Some Mechanisms of Their Formation. *Dyn. Atmos. Ocean.* **1992**, *16*, 279–304. [CrossRef]
45. Ermakov, S.; Dalilicheva, O.; Kapustin, I.; Shomina, O.; Sergievskaya, I.; Kupaev, A.; Molkov, A. Film Slicks on the Sea Surface: Their Dynamics and Remote Sensing. In Proceedings of the IEEE International Geoscience and Remote Sensing Symposium, Waikoloa, HI, USA, 26 September–2 October 2020; pp. 3545–3548. [CrossRef]
46. Sergievskaya, I.A.; Ermakov, S.A.; Ermoshkin, A.V.; Kapustin, I.A.; Shomina, O.V.; Kupaev, A.V. The Role of Micro Breaking of Small-Scale Wind Waves in Radar Backscattering from Sea Surface. *Remote Sens.* **2020**, *12*, 4159. [CrossRef]
47. Dalilicheva, O.; Sergievskaya, I.; Ermakov, S.; Shomina, O.; Kupaev, A.; Kapustin, I. A study of relation between non-Bragg microwave radar backscattering and decimeter-scale wind waves. In Proceedings of the SPIE, Remote Sensing of the Ocean, Sea Ice, Coastal Waters, and Large Water Regions, online Spain, 13–18 September 2021. [CrossRef]
48. Ermakov, S.A.; Kijashko, S.V. Laboratory study of the damping of parametric ripples due to surfactant films. In *Marine Surface Films*; Gade, M., Hühnerfuss, H., Korenowski, G.M., Eds.; Springer: New York, NY, USA, 2006; pp. 113–128; ISBN 3-540-33270-7. [CrossRef]
49. Huang, N.E.; Tung, C. The dispersion relation for a nonlinear random gravity field. *J. Fluid Mech.* **1976**, *75*, 337–345. [CrossRef]
50. Phillips, O.M. *Dynamics of Upper Ocean*, 2nd ed.; Cambridge University Press: Cambridge, UK, 1977; p. 336.
51. Hughes, B.A. The effect of internal waves on surface wind waves. 2. Theoretical analysis. *J. Geophys. Res.* **1978**, *83*, 455–469. [CrossRef]
52. Plant, W.J. A relationship between wind stress and wave slope. *J. Geophys. Res.* **1982**, *87*, 1961–1967. [CrossRef]